

# Exploring Influences of Shallow Topography in Stable Boundary Layers

## The SAVANT Field Campaign

April Hiscox, Sudheer Bhimireddy, Junming Wang, David A. R. Kristovich, Jielun Sun, Edward G. Patton, Steve P. Oncley, and William O. J. Brown

**ABSTRACT:** Stable boundary layers are still a relatively problematic component of atmospheric modeling, despite their frequent occurrence. While general agreement exists that Monin–Obukhov similarity is not applicable in the stable boundary layer (SBL) due to the nonhomogeneous, nonstationary flow, no universal organizing theory for the surface SBL has been presented. The Stable Atmospheric Variability and Transport (SAVANT) field campaign took place in the fall of 2018 to explore under what conditions shallow drainage flow is generated. The campaign took place in an agricultural setting and covered the period of both pre- and postharvest, allowing for not only a basic exploration of the boundary layer but also a robust dataset for applied agricultural understanding of aerosol dispersion and impacts of changes in surface cover on drainage flows. This article provides a description of the field campaign. Examples of publicly available data products are presented, as well as examples of shallow drainage flow and corresponding lidar measurements of dispersion. Additionally, the field campaign was used to provide educational opportunities for students from several disciplines, and the outcomes of these joint educational ventures are discussed as models for future collaborations.

**KEYWORDS:** Land surface; Drainage flow; Turbulence; Boundary layer; Diurnal effects; Field experiments

<https://doi.org/10.1175/BAMS-D-21-0332.1>

Corresponding author: April Hiscox, hiscox@sc.edu

Supplemental material: <https://doi.org/10.1175/BAMS-D-21-0332.2>

In final form 19 December 2022

© 2023 American Meteorological Society. This published article is licensed under the terms of the default AMS reuse license. For information regarding reuse of this content and general copyright information, consult the AMS Copyright Policy ([www.ametsoc.org/PUBSReuseLicenses](http://www.ametsoc.org/PUBSReuseLicenses)).

**AFFILIATIONS:** Hiscox—Department of Geography, University of South Carolina, Columbia, South Carolina; Bhimireddy, Wang, and Kristovich—Climate and Atmospheric Science Section, Division of State Water Survey, Prairie Research Institute, University of Illinois at Urbana–Champaign, Champaign, Illinois; Sun—Northwest Research Associates, Seattle, Washington; Patton—Mesoscale and Microscale Meteorology Laboratory, National Center for Atmospheric Research, Boulder, Colorado; Oncley and Brown—Earth Observing Laboratory, National Center for Atmospheric Research, Boulder, Colorado

It is well understood that at night the atmosphere cools and vertical motions are suppressed. Yet atmospheric models still do not accurately predict stable boundary layers (Holtslag et al. 2013; Lemone et al. 2018). Classic boundary layer texts address the physics of boundary layer stability in considerable detail (e.g., Arya 2001; Garrett 1992; Stull 2001) and much work has focused on narrowing definitions, particularly in the weakly stable category (e.g., Mahrt et al. 2012, 1998; Pfister et al. 2019). Some new modeling frameworks have been developed (Optis et al. 2014) with focuses on specific uses such as identifying the minimum wind speed required for sustained turbulence (van de Wiel et al. 2012b) and simplifying stability classifications for use in the field of wind energy (Basu 2018). From a theoretical perspective, it is understood that the traditional stability measures [i.e., the Monin–Obukhov stability parameter ( $\zeta$ ) or Richardson number ( $Ri$ )] are not applicable for horizontally heterogeneous flows. In part it is because turbulent mixing consists of large coherent eddies that are not captured in the scale of the local gradients in Monin–Obukhov similarly theory (MOST) (Sun et al. 2016). In these conditions, bulk measures appear to be more useful, particularly when viewed in conjunction with aerosol measurements. For example, Miller et al. (2012) used a surface bulk temperature difference, which was closely related to the short-term dynamics of aerosol drift.

Despite this understanding, an adequate replacement for MOST has not yet been identified, and several other theories such as local similarity (Optis et al. 2014), multipoint Monin–Obukhov similarly theory (Tong and Ding 2019), and the inclusion of anisotropy (Stiperski and Calaf 2018; Stiperski et al. 2019) have been developed and show promise in heterogeneous terrain. The hockey-stick theory (HOST) describes turbulence generation in stable conditions over nonhomogeneous conditions and has been tested theoretically by several authors (e.g., Grisogono et al. 2020; Kaiser et al. 2020) and experimentally for many different situations (Acevedo et al. 2019; Andreas et al. 2012; Pfister et al. 2021a,b; van de Wiel et al. 2012a). It is clear that understanding specific characteristics of nocturnal flows is essential to develop a robust modeling framework. Toward this end, our knowledge of flows in stable boundary layers has increased beyond that for the simplest case of open flat areas (Grisogono and Oerlemans 2001; Kurbatskii and Kurbatskaya 2011; Sun et al. 2020; Svensson and Holtslag 2009).

It is also known that stable air stratification can result in katabatic downslope winds, even in very shallow topographic airsheds. Field studies such as MATERHORN (Pardiyak and Leo 2020) and Perdigão (Fernando et al. 2019) have allowed study of the role of stability in high relief (Cheng et al. 2020), predictability of fog (Gultepe et al. 2016), and a terrain gap (Vassallo et al. 2021). Other campaigns, such as SABLES-98 (Cuxart et al. 2000) and CASES-99 (Poulos et al. 2002) were intended to focus more specifically on the stable boundary layer without terrain effects, and are generally considered homogeneous, although a single gully at the

CASES-99 site did provide insight into drainage flows (Soler et al. 2002) and showed up-gully flows can produce gravity waves (Balsley et al. 2002). Still other campaigns such as LAFE (Wulfmeyer et al. 2018) and BLLAST (Lothon et al. 2014) have further shown both the deficiencies of MOST (Lee and Buban 2020) and the dependence of HOST on orographic features (Yus-Díez et al. 2019).

In general, these works have focused on the extreme ends of the topographic spectrum and little attention has been paid to the more common shallow topographies that dominate the central United States and other regions around the globe. These areas are neither homogeneous nor are they completely flat, as they are often broken into areas of different crop covers and contain waterway drainage pathways. A notable exception is the shallow valley work of Mahrt et al. (2014b) in the Shallow Cold Pool Experiment (SCP), which has shown the complexities of these flows (Mahrt 2017), and further highlighted the difficulty of modeling stable layers in low wind speeds (Lapo et al. 2019). Yet identifying causal mechanisms of nocturnal events such as these downslope flows is still difficult (Fernando et al. 2019, 2015; Mahrt et al. 2015; Vassallo et al. 2021). Finnigan et al. (2020) provide a complete review of our current understanding of boundary layer flows over complex terrains and acknowledge that a major limitation to prediction of gravity driven flows is the lack of reliable parameterizations of turbulent mixing, particularly in weak-wind conditions.

Drainage flows are known to be important factors in turbulence generation over deep valleys and gentle slopes (Acevedo and Fitzjarrald 2003; Clements et al. 1989; Fernando et al. 2019, 2015; Mahrt et al. 2015; Vassallo et al. 2021). Drainage flows can occur in sloping terrain when negative surface heat fluxes or other nonuniform turbulent heat fluxes give rise to variations in boundary layer air density and pressure. At higher altitudes, motion initiates due to negative buoyancy of the near-slope air with surrounding air at the same altitude (Doran et al. 1990; Whiteman 2000) with a steady state being reached when “the continuous loss of heat to the surface is balanced by continuous compressive heating” (Smith 2019). However, many studies identified drainage flows that are much more complex than that expected by this simple conceptual model (e.g., Hoover et al. 2015; Mahrt 2017; Mahrt et al. 2010; Medeiros and Fitzjarrald 2014).

In regions of shallow topography, which is predominate in the agricultural regions of the central United States, drainage flows can be quite shallow (Lemone et al. 2018) with wind speeds only reaching up to 1 or 2 m s<sup>-1</sup>. With a wind speed maximum sometimes occurring at heights of only a few meters above the surface, this can give rise to unexpectedly strong shear stress, for environmentally light winds, near the surface (Mahrt et al. 2014a; Nadeau et al. 2013; Pfister et al. 2021a,b). Shallow topography of this nature is particularly of interest from an applied perspective as it represents a large agricultural/cropping area for the United States, and concerns over herbicide and pesticide spraying in stable conditions have escalated in recent years (Gray 2019; USEPA 2022). The Stable Atmospheric Variability and Transport (SAVANT) field campaign sought to address this issue through a comprehensive combination of remote and in situ observations.

In reality, airsheds at any scale are not spatially homogenous nor are they steady state at night. This is due to nonstationary and nonuniform radiative cooling and evolution of the flow believed to promote intermittent turbulence. From a practical standpoint, stable conditions generally result in surface emissions of aerosols and particulates remaining clumped in meandering plumes moving near the ground with little vertical dispersion. Thus, concentrations in the downwind path can be orders of magnitude higher than during daytime unstable conditions when the material disperses vertically into a much deeper layer of the atmosphere (including the residual layer and entrainment zone above). Even though the stable boundary layer is normally shallow, internal gravity waves (IGW) can propagate at an angle from the horizontal plane and modify local shear to generate periodic turbulent mixing

(Sun et al. 2015). SAVANT data provide a means to understand how flows and waves in modest topography interact, causing complexities that are not adequately simulated.

The long-term objective of the SAVANT field campaign was to quantify the effects of shallow cold-air drainage/convergence on aerosol transport and dispersion. The first step of this was to identify under what conditions these converging flows may exist. In this manuscript we present an initial classification based on along-gully wind speed conditions and an assessment of how a dramatic change in surface roughness impacts the potential for terrain influenced flows. More specific impacts such as the identification of specific drainage flows, convergence at intersecting gullies, interactions with larger mesoscale flows, the quantification of spatial scales, and model parameterizations are the subject of future more in-depth investigations, which can be made from the available data.

The campaign took place in the fall of 2018 in central Illinois. This paper provides an overview of the SAVANT field campaign, its scientific objectives, and describes the data source now available to the research community at large to help answer the wide range of questions that exist about flows in shallow topography. Data collected during the SAVANT campaign comprise a comprehensive dataset of key variables related to the formation and progression of drainage and converging flows along a main gully with potential interactions from feeder gullies. A unique combination of remote and in situ measurements addressed both the temporal and spatial aspects of the flows. Aerosol plumes were used as tracers of the flows at the experimental site. The campaign took place in an agricultural setting and covered the period of both pre- and postharvest, allowing not only a basic exploration of the boundary layer, but providing a robust dataset for applied agricultural understanding. Additionally, the field campaign was used to provide educational opportunities for students from several disciplines and the outcomes of these joint educational ventures will be discussed as models for future collaborations.

## Site description

The campaign took place just north of Mahomet, Illinois ( $40^{\circ}12'41.46''\text{N}$ ,  $88^{\circ}24'37.99''\text{W}$ ). The primary instrumented site is a 116-acre ( $0.67\text{-km}^2$ ) agricultural field used for corn and soybean cultivation. The field has shallow-slope topography with a maximum change in elevation of 10 m, predominately from east to west. The terrain ruggedness index (TRI) over the entire extent of the field site is 79 m. TRI can be computed in all GIS programs, and it is used to compare the sum change in elevation between each grid cell with its surrounding neighbors. That comparison is then averaged over the whole field site. This places the topography just within the “nearly level” range ( $\text{TRI} = 0\text{--}80\text{ m}$ ) as defined by Riley et al. (1999). A narrow, shallow-slope main gully runs across the site, into which several, smaller “feeder gullies” intersect. The average vectorized ruggedness measure (VRM) (Sappington et al. 2007) along the gully path is 0.0003. VRM values can range from 0 to 1, with 0 being completely flat and 1 being most rugged (Sappington et al. 2007).

The main gully (MG in Fig. 1) was instrumented with four towers (Figs. 1 and 2) along the anticipated drainage pathway. The location for each tower was selected to represent distinct zones in the anticipated drainage regime. The initiation of flow was expected at the highest point along the gully, just east of a road and at the starting point of the main gully (Init in Fig. 1). A 10-m-tall Integrated Surface Flux System (ISFS) tower dubbed “initiation tower” was placed at this location ( $40^{\circ}12'41.4576''\text{N}$ ,  $88^{\circ}24'37.98''\text{W}$ ). The second tower was called the “release tower” and was a 20-m ISFS tower located 297 m down-gully from initiation. It was located at a slight curve in the gully (Rel in Fig. 1,  $40^{\circ}12'42.1596''\text{N}$ ,  $88^{\circ}24'26.046''\text{W}$ ). The location of this tower was where tracer smoke (Chauvet Professional Atmos Fogger, Sunrise, Florida) was released during intensive operations periods (IOPS). A third tower with a height of 10 m was installed (UConv in Fig. 1,  $40^{\circ}12'39.783''\text{N}$ ,  $88^{\circ}24'19.605''\text{W}$ ). This tower was



named “upper convergence” and was intended to measure converging flow from the main gully and a secondary gully FG1 (Fig. 1). The fourth tower was named “lower convergence” (LConv in Fig. 1, 40°12′36.9″N, 88°24′13.3″W). It was 20 m tall and located ~158 m from the upper convergence tower, at the point where another secondary gully (FG2) joined the

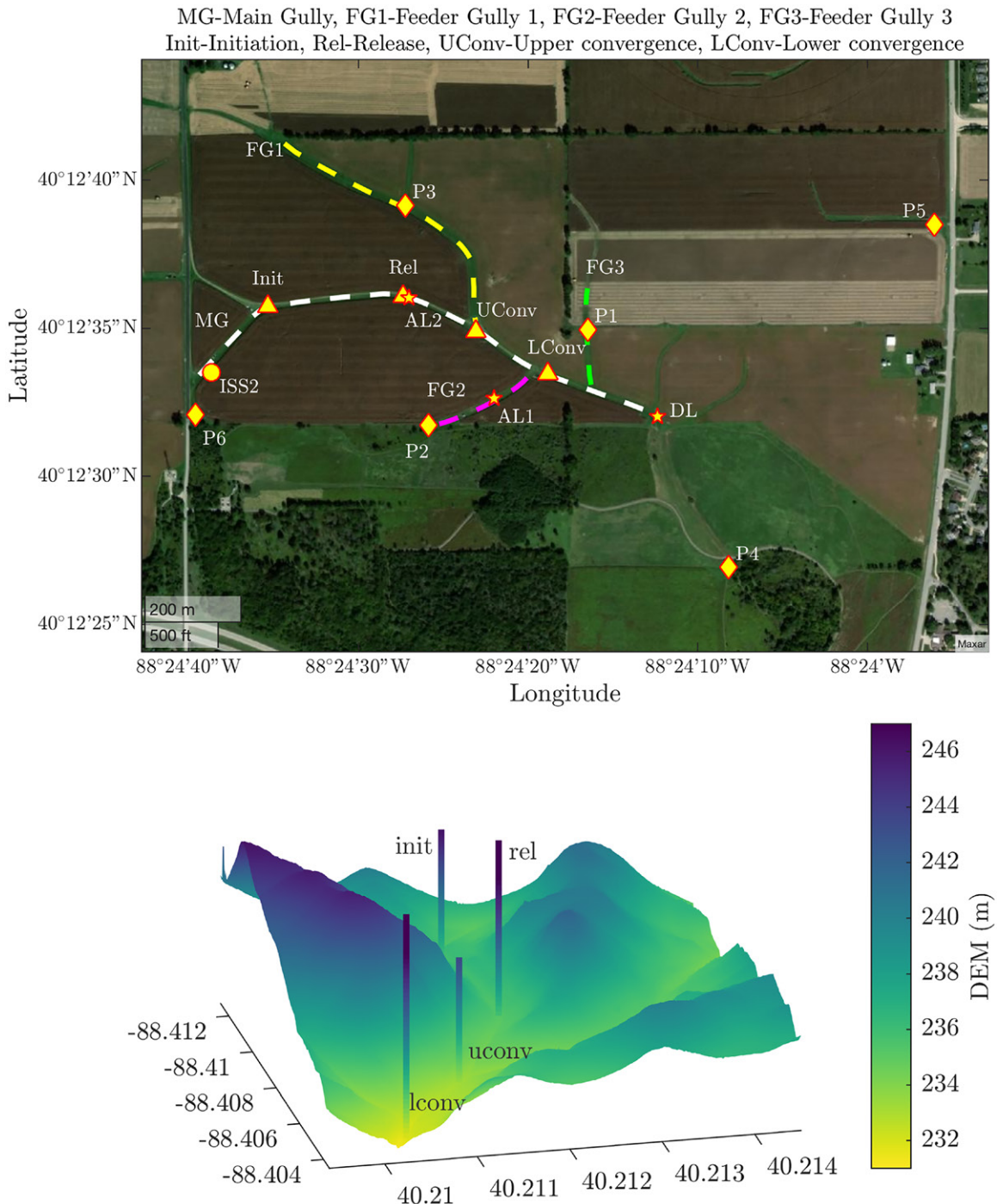


Fig. 1. (top) SAVANT field setup: dashed line represents the gully pathways. MG: main gully (white dashed line); FG1: feeder gully 1 (yellow dashed line); FG2: feeder gully 2 (magenta dashed line); FG3: feeder gully 3 (green dashed line). Tower locations are represented by triangles. Init: 10-m-tall initiation tower; Rel: 20-m release tower; uconv: 10-m upper convergence tower; lconv: 20-m lower convergence tower. Diamonds represent locations of atmospheric pressure sensors P1–6. All towers and pressure sensors were part of the Integrated Surface Flux System (ISFS). Stars represent lidar locations. AL1: aerosol lidar 1; AL2: aerosol lidar 2; DL: Doppler lidar; the circle represents the location of the Integrated Surface Sounding System (ISS2) trailer, which contained the sodar and ceilometer. (bottom) 10-cm-resolution digital elevation model (DEM) of field site with tower locations denoted.

main gully. The elevation continued to decrease for some distance offsite beyond the Doppler lidar, where two pressure stations (P4 and P5) were located.

Figure 2 shows the arrangement of measurements made at each tower. Each tower was equipped with CSAT3 sonic anemometers at multiple heights ( $U$  as representative of  $u$ ,  $v$ , and  $w$  wind components) and aspirated temperature and relative humidity sensors ( $T$ ,  $RH$ ). At 20 cm above ground 2D sonic anemometers were placed ( $u$ ,  $v$ ). Radiation and soil budget variables were measured at three of the towers, these were soil temperature ( $T_s$ ), soil moisture ( $Q$ ), and soil heat flux ( $G$ ). In addition, during IOPS, towers were equipped with DustTrak (DT) and/or optical particle counters (OPC) to track the released smoke. Each of the four main towers was augmented with two shorter (1.5-m) auxiliary towers equipped with CSAT3 sonic anemometers and aspirated temp/RH sensors to measure cross-gully wind changes. These are not shown in Fig. 1 or Fig. 2 but were installed toward the edge of the gully in a line perpendicular to the main gully orientation approximately 5 m away. All the main tower-based instruments are listed in Table 1 and additional details are available from the EOL data archive ([www.eol.ucar.edu/content/isfs-savant](http://www.eol.ucar.edu/content/isfs-savant)). Sonic anemometer observations were recorded at 20 Hz, and all other tower-based sensors sampled at 1 Hz or faster when the instrument allowed. Six microbarographs were also deployed in a nested triangular configuration (P1–P6 in Fig. 1). These measured pressure at a rate of 1 Hz and were intended to identify internal gravity wave activity across the site.

In addition to these point measurements, SAVANT utilized several spatially flexible instruments. Three ground-based lidars were deployed and represented the heart of the SAVANT IOPS. Two of these lidars were aerosol scanning systems from Raymetrics Lidar Systems (Athens, Greece), and the third was a Doppler lidar (Halo Streamline XR from Halo Photonics, United Kingdom). All three lidars can provide multiple measurement configurations and

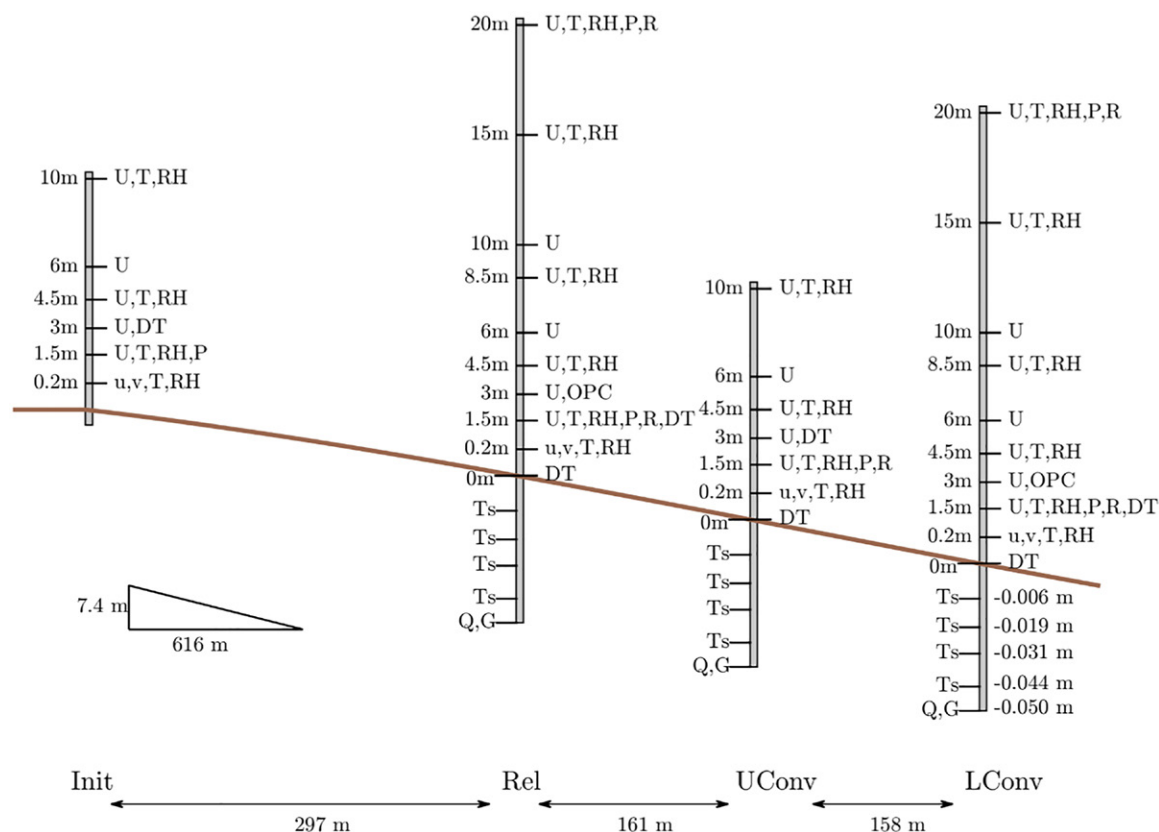


Fig. 2. Location of measurements on each tower.  $U$ : 3D wind velocities measurements;  $T$ : air temperature;  $RH$ : relative humidity;  $DT$ : DustTrak;  $u$ ,  $v$ : horizontal wind components from 2D sonic anemometers;  $P$ : pressure measurement;  $R$ : four-component solar radiation measurements;  $OPC$ : optical particle counter;  $T_s$ : soil temperature;  $Q$ : soil moisture;  $G$ : soil heat flux.

**Table 1. Instruments at SAVANT.**

Variable	Instrument	Additional details
Plume size, shape, relative spatial concentrations	Ground-based aerosol scanning lidars (RAYMETRICS LB100)	Lidar 1 (AL1): 3.75-m resolution, 20 Hz provided by University of Illinois Lidar 2 (AL2): 7.5-m resolution, 20 Hz provided by University of South Carolina Locations in Fig. 1
Doppler wind fields and profiles; plume dispersion	HALO Streamline XR Doppler lidar (DL)	5 Hz, 18-m range resolution; location in Fig. 1
Particle concentration	DustTrak (TSI 8520 and TSI 8530) (DT)	1 Hz, point data
Particle size distribution	Optical particle sizer (TSI 3330, OPC)	1 Hz, point data
Wind speed, direction, and turbulence parameters	Sonic anemometers (CSAT3 for $u$ , $v$ , and $w$ , Gill 2D for $U$ )	3D anemometers at most locations, 2D at 20-cm height AGL
Fast water vapor	Infrared gas analyzers	20 Hz, two on each tower at 0.5- and 5-m heights; not shown in Fig. 2
Surface energy balance	Net radiometer ( $R$ ), soil temperature ( $T_s$ ), heat flux plate ( $G$ ), soil moisture ( $Q$ )	1 Hz, one at top and one at bottom of each of the three towers
Cloud cover	Moonglow Technologies All Sky Cam ASC-N1 SS All-Sky Camera	Images saved every 5 min, <a href="https://doi.org/10.26023/T7AX-F06C-C501">https://doi.org/10.26023/T7AX-F06C-C501</a> Located at ISS2 in Fig. 1
Cloud-base and backscatter layers	Vaisala CL51	<a href="https://doi.org/10.26023/FCH1-5AVT-QV0E">https://doi.org/10.26023/FCH1-5AVT-QV0E</a> Located at ISS2 in Fig. 1
Horizontal wind environment	NCAR/EOL 449 MHz Modular Wind Profiler	5- and 30-min winds <a href="https://doi.org/10.26023/K6J3-MJG4-RG0D">https://doi.org/10.26023/K6J3-MJG4-RG0D</a> Located at Homestead site
Air pressure	Vaisala PTB220 digital barometers	Measured at 1 Hz, locations P1–6
Above-surface pressure	Paroscientific nanobarometers	0.5 and 20 m at Rel, 10 Hz 1.5 and 20 m at LConv, 10 Hz
Along-gully temperature	CTEMPS DTS	Main gully at 0.2-m height, 1 Hz, 12.5-cm resolution along the cable

customizable scanning routines to produce time and space resolved measurements of the boundary layer. During SAVANT IOPS, one Raymetrics system (AL2 in Fig. 1) was located near the release tower and conducted vertical (RHI) scans along the gully. The second Raymetrics system (AL1 in Fig. 1) was positioned midway down feeder gully 2 and it performed a combination of “cross-gully” RHI scans and very narrow side to side (PPI) scans near the surface of the areas surrounding the lower convergence tower. Specific scan angles were controlled by the lidar operator in real time to most closely track the smoke plume during each individual IOP. The Doppler lidar (DL in Fig. 1) was located at the lowest point of the field and conducted PPI scans over the entire site. Figure 3 shows the scanning paths and an example of the three systems working together during an IOP.

A distributed temperature sensor (DTS) from the Center for Transformative Environmental Monitoring Programs (CTEMPS) was also deployed (De Jong et al. 2015). The DTS-CTEMPS cable was mounted 20 cm above the ground and ran the length of the main gully, zigzagging around each tower site. DTS-CTEMPS was activated during all IOPS with a sampling rate of 2 s and a spatial resolution of 0.127 m. The full length of cable installed was ~500 m; however, the thin, near-surface cable was difficult to maintain, so reliable data are only available for IOPS along the upper portion of the gully (ISS2 to Init to Rel in Fig. 1).



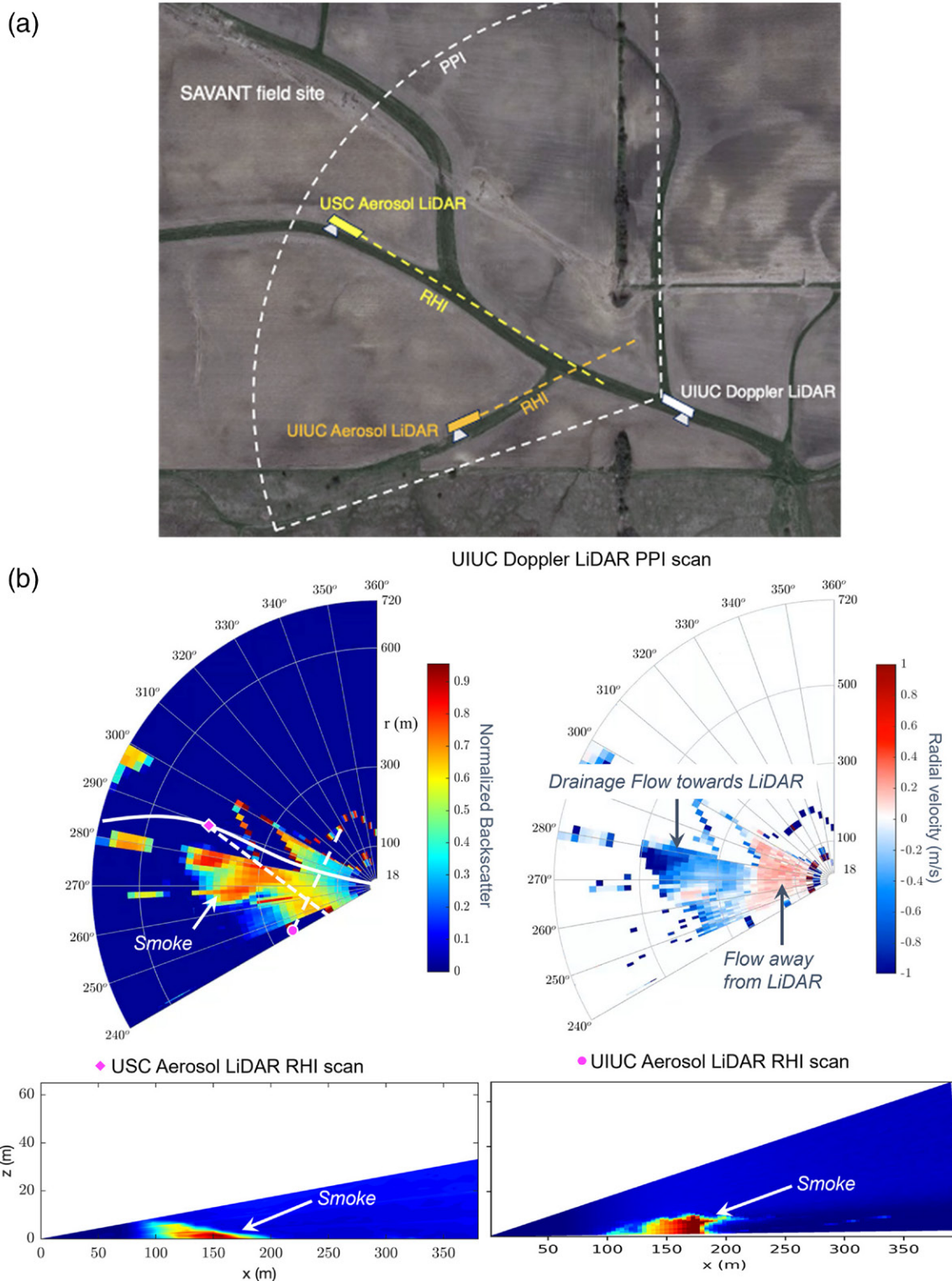


Fig. 3. Data from the three lidars during SAVANT taken at 2125 CDT (Doppler), 2114 CDT (UIUC Aerosol), and 2120 CDT (USC Aerosol) 2 November 2018. All three lidars scanned a released plume. (a) Lidar locations and scan angles. (b) (top) Aerosol data and winds from the Doppler lidar scan, which took a near-horizontal (PPI) scan above the full measurement site. Diamond magenta marker corresponds to the USC lidar, and circle magenta marker shows the UIUC Aerosol lidar location. The approximate sight-lines for the Aerosol lidar scans are overlayed on the plot as white dashed lines. The thick white solid line corresponds to the main gully. The Doppler PPI scan was performed at an elevation angle of  $1.5^\circ$ . (b) (bottom left) A vertical (RHI) slice along-plume centerline and (b) (bottom right) the vertical slice across the plume axis. The two RHI scans intersect each other perpendicularly at  $\sim 200$  m on the x axis.



In addition to the data presented here, several additional sensors and datasets are available. National Center for Atmospheric Research (NCAR) Integrated Surface Soundings (ISS) facilities were deployed to measure vertical profiles of atmospheric characteristics. Two locations were used. A trailer located at ISS2 served as the base for a sodar, site power, on-site data access station, housed an all-sky camera, a ceilometer, and served as the origin point for the CTEMPS-DTS. This was near the highest elevation point in the southeast corner of the site (ISS2 in Fig. 1). A secondary site called ISS Homestead (40°13'31.7994"N, 88°27'42.9984"W) was located 4.5 km (2.8 mi) west of the main site. This site was the location for a 449-MHz profiler, NCAR ISFS and ISF base trailers, and a 10-m standard meteorological tower. It also served as the launching point for balloons during IOPS. Table 1 summarizes all the measurements made during the campaign.

### Data availability and IOPS

A 2-month campaign in the fall season captured a variety of atmospheric conditions, as well as preharvest and postharvest surface characteristics to elucidate to what extent changes in surface cover can alter drainage conditions. ISFS and ISS instruments (instruments on towers, pressure sensors, 449-MHz profiler, ceilometer, and sodar) continuously collected observations 24 h per day from 19 September to 15 November 2018. This manuscript focuses on the nocturnal data. In total, the full suite collected nocturnal data on 65 nights between 19 September and 24 November. For the purposes of the remainder of the work presented here, nighttime is defined as times between 1900 and 0600 local time. This encompassed night throughout the campaign. Sunrise time varied from 0637 LT 19 September to 0648 LT 24 November and sunset ranges from 1854 LT 19 September to 1630 LT 24 November. It should be noted that daylight saving time ended during the study (4 November), so this should be considered by researchers using SAVANT data although the time zone in logged data files was not changed. In the analysis presented below, only 5-min data are presented (NCAR/EOL 2021). In addition, the nights of 11–14 October were removed from all the results. The field was being harvested over these dates, so canopy conditions were variable. These data are available in the EOL archive for further analysis on the effects of changing surface cover but are not included in the analysis presented here.

Thirteen intensive operations periods were conducted during nocturnal conditions. This includes one dry run to ensure field operation practices were well-established. During these periods, tracer smoke was released several meters up-gully from the release tower (just west of the star in Fig. 1) and DustTrak/Optical Particle Sizer observations were taken at intervals of 1 s on all four towers (heights are noted in Fig. 2). Lidars were run during IOPS, although AL2 was only active for the last 4 IOPS (unfortunately, the laser was damaged in transport and unavailable for earlier IOPS). Sounding balloons (Vaisala MW41/RS 41 radiosondes) were launched every 3 h during IOPS. All the IOPS and their general characteristics are summarized in Table 2. Field reports were written for every IOP and are available in the SAVANT field catalog (<http://catalog.eol.ucar.edu/savant>). The completed IOPS covered nights of clear, partly cloudy, and overcast skies with generally weak synoptic winds. Among the 12 IOPS, 3 were preharvest with full crop cover, 1 was during a partial harvest, and the remaining 8 were postharvest.

To determine timing for IOPS, a team of students led daily microforecasts, which were broadcast live via a public web link at 1500 local time (LT). The primary forecast goal was to ascertain the likelihood of overnight atmospheric conditions favorable for drainage flow. Such forecasts provided a useful experience for the students, allowed for group discussions of whether favorable conditions were expected and, if so, the time of intensive operations, and allowed for logistical planning for up to 5 days in advance. Favorable forecasted conditions included statically stable near-surface boundary layers, light to calm winds below 10 m,

**Table 2. Summary of IOPS.**

IOP No.	Time (local/central time)	Instruments	Visual notes on smoke movement	Additional notes
1	2130 LT 23 Sep to 0230 LT 24 Sep 2018	Towers, profilers, AL1, DL, balloons, DTS	No down-slope flow seen	Dry run
2	2200 LT 29 Sep to 0130 LT 30 Sep 2018	Towers, profilers, AL1, DL, balloons, DTS	No down-slope flow seen	—
3	0100 to 0700 LT 12 Oct 2018	Towers, profilers, AL1, DL, balloons, DTS	Down-gully flow is slow and smoke meanders cross-gully	Corn north of gully had been harvested prior to start of observations. Corn south of gully still present. Harvesting corn south of gully began at 0615 LT.
4	1123 LT 15 Oct to 0630 LT 16 Oct 2018	Towers, profiler, AL1, DL, balloons, DTS	Brief intermittent drainage	Some smoke meandering was observed between 0000 and 0100 LT.
5	2230 LT 17 Oct to 0700 LT 18 Oct 2018	Towers, profilers, AL1, DL, balloons, DTS	Frequent drainage flows	Smoke filled up the whole experimental site (like a basin from the gully bottom up to the top of the local terrain). The flow appeared stratified to different layers.
6	2200 LT 23 Oct to 0700 LT 24 Oct 2018	Towers, profilers, AL1, DL, balloons, DTS	Shallow and oscillated drainage	Soybean field was harvested before this IOP.
7	2000 to 2300 LT 27 Oct 2018	Towers, profilers, AL1, DL, balloons, DTS, AL2 run in repair/alignment mode	Shallow and oscillated drainage	The drainage flow established early, with a layer of smoke staying above ground. Change in flow to up-gully around 2200 LT, with increase in large-scale winds.
8	1800 LT 30 Oct to 0100 LT 31 Oct 2018	Towers, profilers, AL1, DL, balloons, DTS, AL2 run in repair/alignment mode	Down-gully flow established early, with a layer of smoke staying above ground	Around 2200 LT as large-scale winds increase, flow changed to up gully.
9	1800 LT 1 Nov to 0700 LT 2 Nov 2018	All	Intermittent drainage	Initial drainage was observed at upper convergence at 1934 LT with the longest and clearest period of drainage before midnight.  Other notable periods of drainage were just after midnight and 0430 to 0545 CDT.
10	2000 to 2330 LT 7 Nov 2018	All	No down-slope flow seen	It was too windy ( $5 \text{ m s}^{-1}$ or more at most towers), so IOP concluded early.
11	1630 to 2020 LT 10 Nov 2018	All	No down-slope flow seen	—
12	1800 LT 11 Nov to 0000 LT 12 Nov 2018	All	An extremely brief period of drainage was observed	Inversion layer was shallow.
13	0100 to 0730 LT 14 Nov 2018	All	Brief periods of drainage in early morning hours	A thin layer of snow was on ground before and during this IOP.

clear skies, and low boundary layer shear. This provided the best opportunity to observe the flows under various forcing conditions. A forecast grid for the upcoming 5-day period was maintained with a simple color-coded system (yellow—possible IOP; red—no IOP; green—likely IOP). Our experience was that cloud cover was particularly difficult to

forecast for overnight hours and that forecasted winds of stronger than  $3 \text{ m s}^{-1}$  were generally enough to preclude formation of drainage flows.

## Summary observations

**General nocturnal wind conditions.** To understand the general behavior of nighttime winds in stable atmospheric conditions, the dataset was first filtered to remove periods of precipitation. Precipitation periods were identified using leaf wetness sensors (Decagon, Inc., Pullman, Washington) at the top of the two tallest towers. The remaining 6,540 five-minute nocturnal observations were further divided into two regimes to address the main scientific goal of understanding what conditions promote draining and converging flows. We apply a broad definition of drainage here based on a change in wind speed in the main gully at 1.5 m above ground level (AGL). At the SAVANT site, the very shallow, yet complex, topography resulted not only in along-gully drainage flow, but also showed regions of convergence near the intersections of feeder gullies and interactions of larger-scale flows with these terrain induced gully flows, periods of intermittent drainage, and occasional upslope flows. A single criterion for these flows is not possible. The goal of this manuscript is to show how often the types of flows can occur and present the general commonalities under which they exist. Toward that end, we identify periods when near-surface wind speed increased down the gully (i.e., some form of drainage was present) and the change was significantly higher than background (i.e., nongully) flow. Thus, “drainage-likely” conditions were defined using the 1.5 m AGL wind speed at each tower. Any 5-min period was flagged as drainage likely if the wind speed increased from the release tower to the lower convergence tower by more than 10% of the wind speed measured for the same time at the initiation tower ( $U_{\text{conv},1.5} - U_{\text{rel},1.5} > 0.1U_{\text{init},1.5}$ ). All conditions not meeting these criteria were considered “normal”—meaning that no significant direct gully effect was observed at the 1.5-m height. Examining the dataset in this way provides a climatology of conditions and an overview of flow consistency. It should be noted that with this selection method, normal conditions may contain intermittent or turbulent induced drainage events at the sub-5-min time scale. This method is intended to simplify our summary of drainage flows presented here. Separating the data in this way allows us to look at the data in aggregate and is not intended to be a comprehensive definition of drainage, but rather to put some constraints on when drainage conditions can exist.

In total, 2,051 five-minute periods were flagged as drainage likely. This represents 31% of the nocturnal dataset. Fifty of the 56 nights examined have at least one 5-min drainage-likely period. Drainage-likely conditions were more prevalent earlier in the season and prior to harvest (44% versus 25% postharvest). Additionally, generally fewer periods were found in any single night after vegetation was completely removed (average of 33 periods per night versus 56 periods when vegetated). On only six nights, no drainage-likely periods were identified. All six of these nights occurred postharvest. Thirty-seven nights were completely rain-free with varying lengths of drainage-likely conditions. Of these rain-free nights, 15–16 November had no drainage-likely conditions identified, and on the opposite end, the night of 28–29 September had the most drainage-likely periods, which occurred consistently throughout the night (93 periods/70% of the data). These two cases are discussed further below.

Mean wind speed profiles at each tower are shown in Fig. 4 for both drainage-likely conditions and normal conditions. Profiles are further separated into pre- and postharvest periods. Not shown are the average profiles across all nocturnal conditions, which show a textbook logarithmic profile. The preharvest profile (Fig. 4, left two panels) had a slightly different shape than postharvest; the effects of this roughness change are examined in more depth in Bhimireddy et al. (2022). The top two panels of Fig. 4 also show that in drainage-likely conditions as defined above, the wind speed profile at the lower part of the gully ( $U_{\text{conv}}$ —black line)

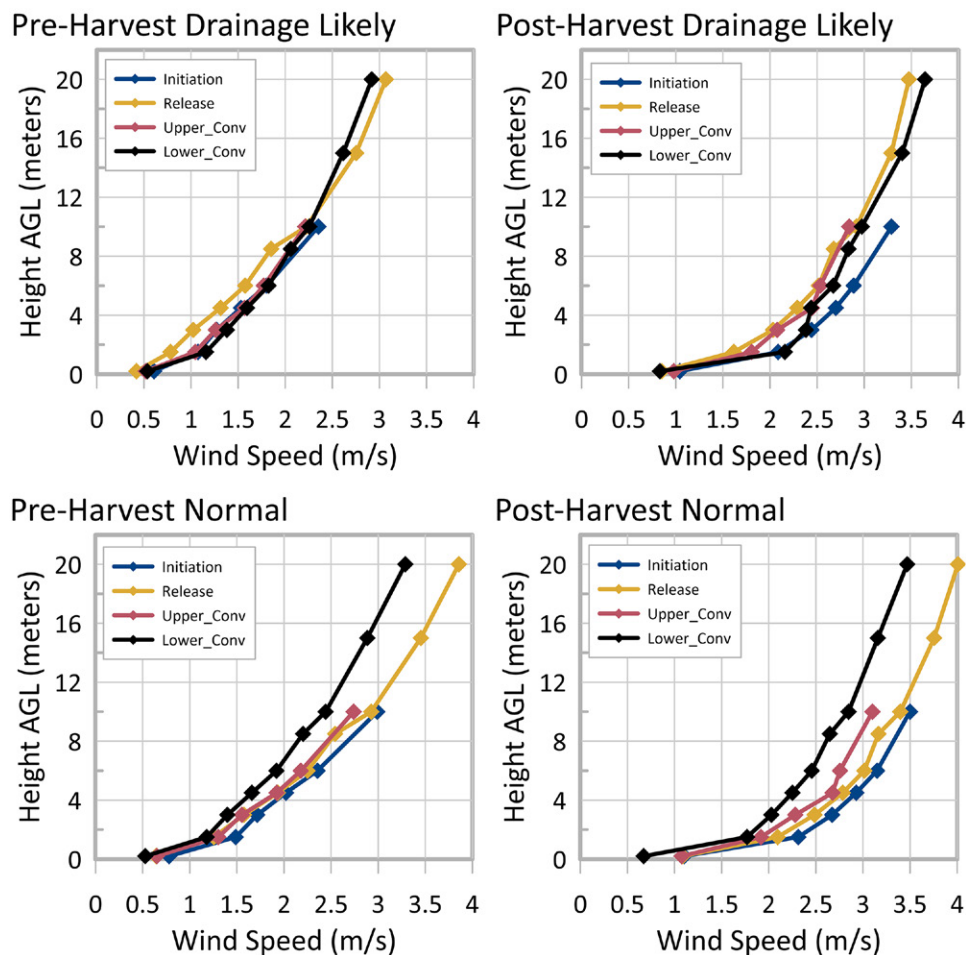


Fig. 4. Mean wind profiles from all four towers. (top) Mean of all drainage-likely observations; (bottom) mean of all other conditions. (left) Preharvest observations; (right) postharvest observations.

was nearly identical with the assumed background profile (init—blue line) in the near-surface layer (<5 m AGL). However, postharvest, the two profiles deviated above this height, while staying the same until 10 m or higher preharvest. The bottom two panels of Fig. 4 show that under normal conditions winds slowed as you move down the main gully, and that the difference is more pronounced after harvest. In all conditions, at all heights, mean winds were always higher postharvest (right panels) when compared to preharvest (left panels). This follows from the reduction of surface friction with the removal of vegetation and may be a seasonal effect. The difference between pre- and postharvest conditions (faster wind speeds), is more pronounced for drainage-likely conditions (upper panels), indicating that vegetation may play a role in promoting conditions favorable to convergence, possibly through channeling the flow. Drainage conditions usually occurred under 10 m AGL. Overall Fig. 4 shows that normal conditions had a consistent pattern, but drainage-likely conditions vary quite a bit more, with phenomena such as pulses, convergences, and meanders complicating the pattern.

An examination of wind directions showed a more complicated environment. Preharvest wind directions are not shown because they follow a consistent pattern: At 0.2 m AGL, winds directions were dominated by along-gully flow at the release and lower convergence towers, while a more cross-gully flow dominated at the upper convergence tower, and an easterly flow dominated at the initiation tower. Within the corn canopy (1.5–6 m AGL) wind roses display generally the same shape at all towers; at 10 m AGL wind directions were dominated by winds from the south. We conclude that during preharvest conditions, drainage potential is not related to wind direction. The dominance of along-gully directions at the 0.2-m height in the drainage-likely



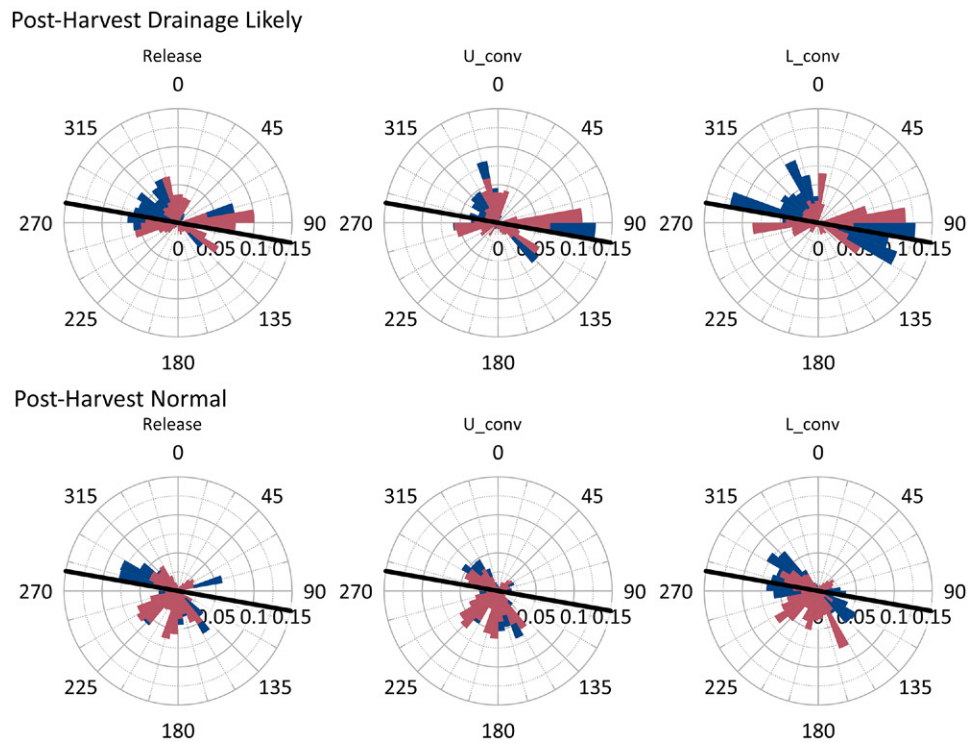


Fig. 5. Distributions of 5-min winds for the three in-gully towers at two heights. Blue boxes are at 0.2 m AGL and red boxes are 10 m AGL. The solid line at 100°–280° represents the approximate gully axis. A larger version with wind roses from preharvest conditions is available in the online supplement (<https://doi.org/10.1175/BAMS-D-21-0332.2>).

conditions confirms that the speed up between the release and lower convergence towers is often, although not always, associated with down-gully flow as instances of up-gully cross-gully winds do exist in the drainage-likely dataset. True drainage would be along the gully from the higher to lower elevation.

Postharvest, the wind direction environment is different. Wind directions for the 0.2 and 10 m AGL heights postharvest are shown in Fig. 5. Postharvest conditions had a less predominant main direction than observed preharvest. At the 0.2-m height, a slightly bimodal distribution existed in the drainage-likely conditions (blue bars, top panel). This near-surface flow aligns most closely with the gully axis at the lower convergence tower. This alignment was not seen at all under normal conditions (blue bars, lower panel).

Interestingly, the 10-m wind direction did vary pre- and postharvest. As mentioned above, preharvest winds were dominated by southerly flow regardless of drainage potential, while few instances of southerly flow were seen in the postharvest drainage-likely data subset (red bars, top panel, Fig. 5). These results highlight the complexities involved in modeling near-surface conditions in shallow terrain and indicate that the SAVANT experiment collected a robust dataset with a wide variety of conditions and case studies available for in depth analysis.

**Example nights (28–29 September, 15–16 November).** For a general understanding of the range of conditions sampled, the nights with the most and least flagged drainage-likely conditions are presented here. The night of 28–29 September had the most drainage-likely conditions throughout the night. We consider this to represent a typical drainage case in which wind speeds increase along the gully path. This night, however, was not an IOP because winds were predicted to increase throughout the night. The night of 15–16 November represents a normal night as no periods were flagged as drainage likely. Both nights were entirely precipitation-free. Figures 6 and 8 show time series of wind speed and inversion strength for

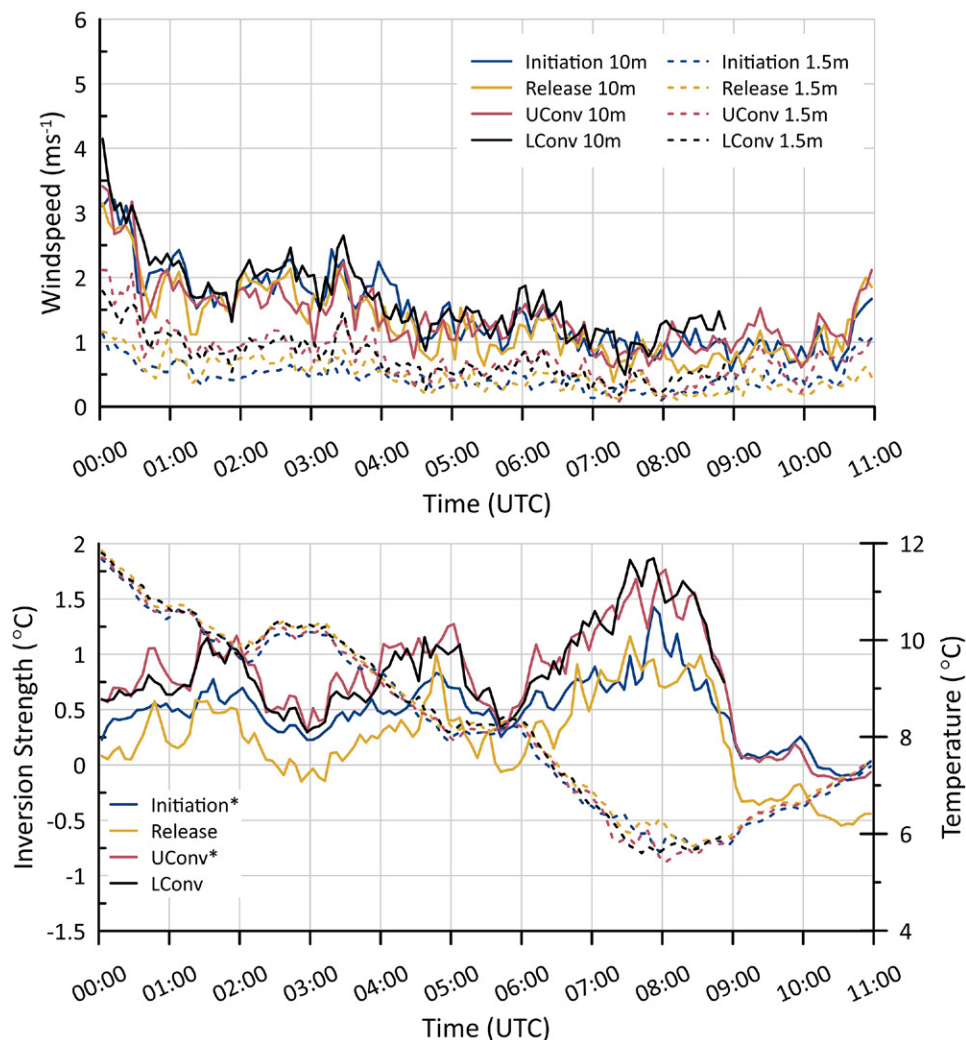


Fig. 6. Time series from drainage-likely night (28–29 Sep); 0600 UTC is midnight local time. (top) The 5-min-average wind speeds at all four towers at heights of 10 m (solid) and 1.5 m (dashed). (bottom) Temperature at 1.5 m AGL (dashed) and inversion strength between 10 and 0.2 m at all towers (solid). Note that temperature was not measured at 10 m directly at the release and lower convergence towers, so values used here are interpolated from the heights above and below. Data presented are from 1900 to 0600 local time. Sunset occurred at 1842 LT (2342 UTC) and sunrise occurred at 0646 LT (1146 UTC).

both example nights, while Fig. 7 shows wind roses for the entire night of 28–29 September separated by tower and height.

There are several notable differences between the two nights. On 28–29 September, within 1 h of sunset, wind speed at 10 m AGL was consistently less than  $\sim 2 \text{ m s}^{-1}$  at all towers, while closer to the surface, at 1.5 m, wind speeds were even slower, rarely exceeding  $1 \text{ m s}^{-1}$  (Fig. 6). The maximum wind speed measured at 0.2 m was  $1.8 \text{ m s}^{-1}$ . Wind directions at 10 m AGL were consistently from the north (Fig. 7), while wind direction at heights in the corn-lined gully was variable with both gully location and height, coming predominately from the northeast at the initiation tower and from the northwest at all other towers. The down-gully flow direction was slightly offset from the gully axis. A few periods of gully alignment did exist at the lower two towers (uconv, lconv) and they occurred later in the nocturnal period, when wind speeds were slower, temperature was cooler, and the inversion was stronger. Apart from the winds measured at the release tower, wind directions did not follow any of the gully pathways exactly but do show the impacts of the feeder gullies at the two convergence towers. With relatively weak ambient winds, variable,

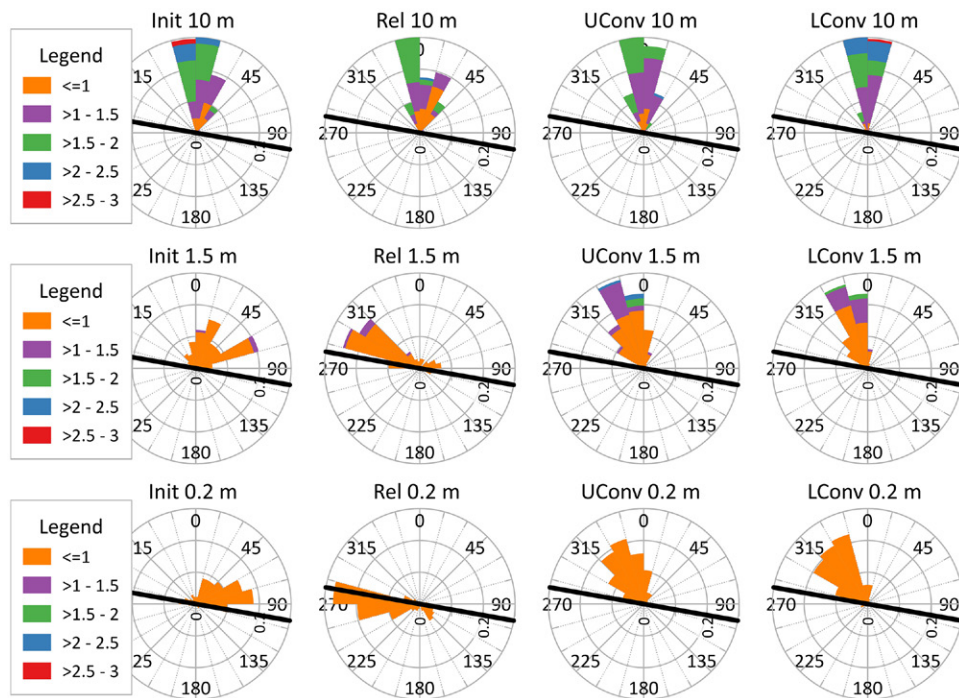


Fig. 7. Wind roses from 1900 LT 28 Sep to 0600 LT 29 Sep, at (top) 10, (middle) 1.5, and (bottom) 0.2 m AGL.

cross-gully winds can exist, at this site there can also be down-gully flow entering the main gully from the feeder gullies. Similar variability in low wind speed conditions have been seen in CASES-99 (Sun et al. 2015). Overall, although the light winds and our selection criteria indicate a high and consistent drainage potential on this evening, the flow did not directly follow the terrain. We believe that in such low wind conditions, ambient direction plays little to no role in drainage potential.

For this example night, temperature shows some variability over the night. This can be seen by examining the lower panel of Fig. 6. Shown in terms of inversion strength (10-m air temperature minus 0.2-m air temperature), we see the atmosphere would be considered stable for the whole evening; however, the strength of the inversion grew and shrank throughout the night. The release tower experienced small periods of near-neutral stability (around 0300 UTC and just before 0600 UTC), and all towers tended toward near neutral after 0900 UTC (0300 local time). During these times, the normal consistent cooling is disrupted briefly at all measurement locations. We also note that the periods on this night that did not meet the criteria for drainage likely as defined above occurred during these same periods of disrupted cooling.

In contrast to the consistent drainage-likely conditions seen on 28–29 September, the night of 15–16 November had zero 5-min periods flagged as drainage likely. This night represents a case of drainage-free conditions where flow is thought to be dominated by larger-scale processes. When examining the whole night, wind speeds were much higher and gustier, rarely falling below  $2 \text{ m s}^{-1}$  except for those measured near the surface at the lower convergence tower (black dashed line, top panel, Fig. 8). The winds on this night were continually from the south at all locations and all heights (not shown). This is consistent with the statistics for the whole campaign postharvest normal conditions discussed above (Figs. 4 and 5). This night would also be considered stable. The onset of an inversion is first seen at the initiation tower then appears at all towers approximately 30 min after sunset, prior to the time shown in Fig. 8.

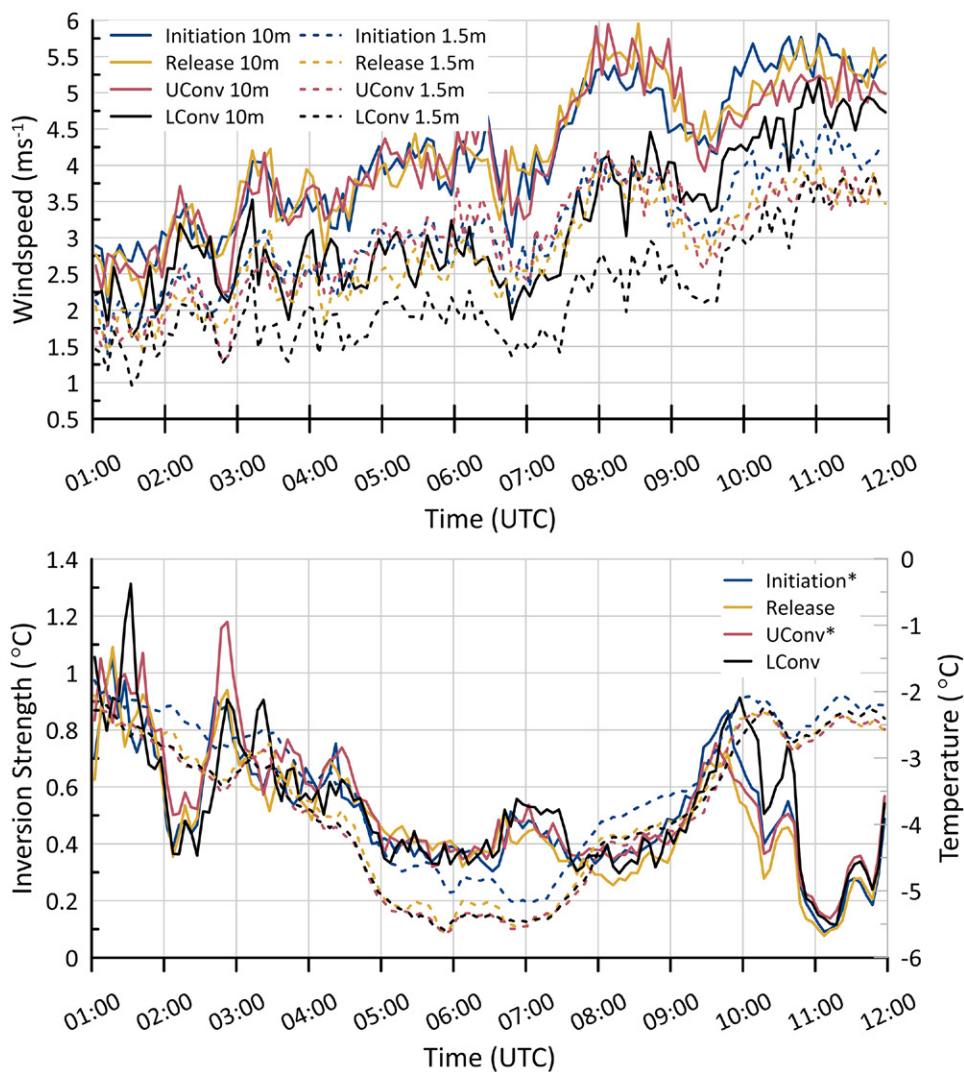


Fig. 8. Time series from 15 to 16 Nov (same as Fig. 6 for normal conditions). (top) 5-min-average wind speeds at all four towers at heights of 10 m (solid) and 1.5 m (dashed). (bottom) Temperature (dashed) and inversion strength between 10 and 0.2 m (solid). Note that temperature was not measured at 10 m directly at the release and lower convergence towers, so values used here are interpolated from the heights above and below. Data presented are from 1900 to 0600 local time. Sunset occurred at 1636 LT (2246 UTC) and sunrise occurred at 0640 LT (1240 UTC).

**Pulsing, converging, and meandering flows.** Within the evenings showing drainage-likely conditions, various types of drainage flows exist. We present here examples of these flows. Traditional drainage flows are initiated once cooling produces dense air at higher altitudes and this dense air continuously moves along a gully, reaching a steady state as the negative heat flux balances the compressional heating of sinking air over the top of the hill (e.g., Smith 2019). Once started, downslope flows can continue even if the negative heat fluxes decrease. However, in SAVANT, pulsed drainage flows, defined as onset of drainage flow with intermittent disruptions throughout the night, were observed from tower data. This is consistent with pulsed drainage in other studies (Doran et al. 2002; Fernando et al. 2013; Mortarini et al. 2016). An example of pulse drainage flow is shown in Fig. 9. Over the night, near-surface cooling rates were consistent; however, drainage flows were observed early, followed by periods of cross-gully flows (i.e., nondrainage) after which drainage flows returned.

Periods with convergence flows are also observed within drainage periods from both tower and lidar data. Figure 10 shows the two convergence types that have been identified in SAVANT. The first is convergence caused by down-gully drainage flow entering stagnant



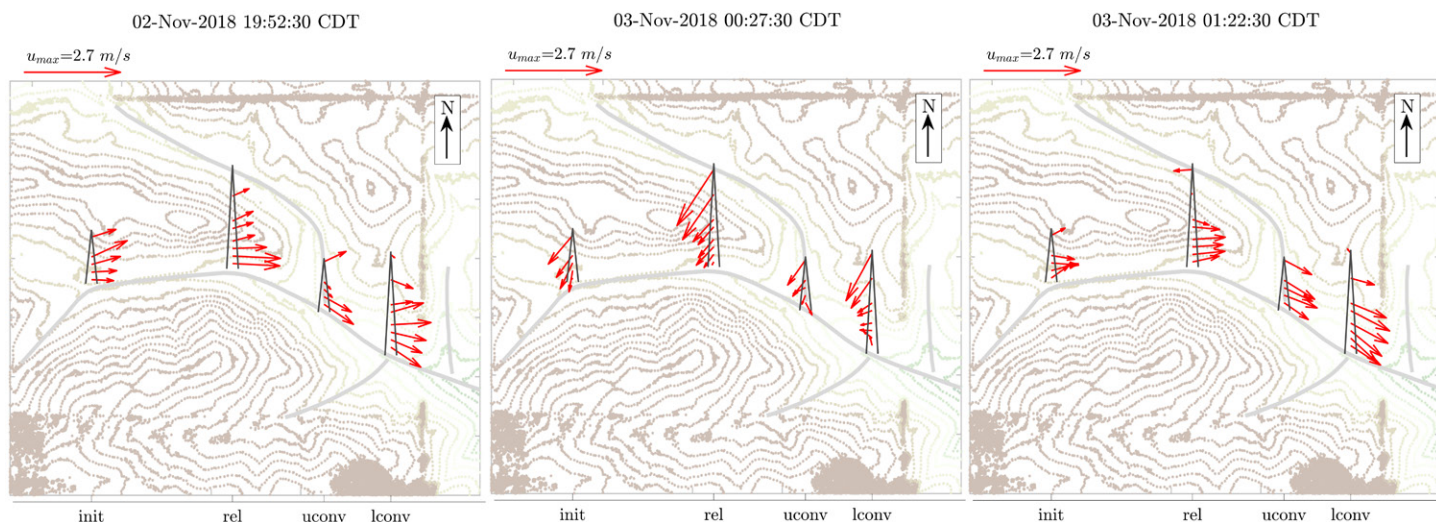


Fig. 9. Example pulse drainage flows on 2–3 Nov 2018. Wind profiles were shown at initiation (init), release (rel), uconv (upper convergence), and lconv (lower convergence) towers at different times as noted in the upper right of each panel: (left) 1952 CDT (drainage flow along main gully), (center) 0027 CDT (nondrainage flow), and (right) 0122 CDT (drainage flow below 15-m height). The wind quivers are scaled with respect to the maximum velocity ( $2.7 \text{ m s}^{-1}$ ).

flow areas (Fig. 10, left). The second is convergence caused when flow from a feeder gully intersects and subsequently disrupts the main-gully drainage flow (Fig. 10, right). The characteristics of the pulse drainage and convergence flows and subsequent effects on the atmosphere are the subject of future research.

### Example spatial observations

In addition to the extensive tower observations, SAVANT used three lidars to obtain spatiotemporal observations of the gully system and adjacent flow fields. Tracer plumes were released during IOP periods and smoke movement was monitored with two aerosol lidars and one Doppler lidar. Figure 3 shows lidar scans from IOP 13 on 14 November. All three lidars were operational from 0100 to 0730 LT on this day. A thin layer of snow was present on the ground and during the IOP drainage-likely data were present for 21% of the night, with almost all drainage-likely periods occurring later in the night when winds became slower.

The Doppler lidar volume scans provided information on the three-dimensional structure of the plume every 10 min. The analysis shown in Fig. 11 gives an example. Contour lines denote the edges of the high-backscatter region indicating the smoke plume. Note that lines that do not enclose a region are for heights in which data were not available for western portions of the sample area. Overall, the plume did not show consistent tilt in a cross-gully direction and aligned with the primary gully. The forward edge of the plume appears to tilt upslope, especially above 10 m or so. This tilt may be somewhat underestimated due to the down-gully movement of the plume with time during the volume scan. The deepest portion of the observed smoke plume is near the lower convergence region during most of the scans taken on this date, suggesting that convergence in this region resulted in a quasi-stationary “hump” in the top of the plume.

### Incorporating teaching

Educational opportunities were a core component of the SAVANT field campaign. Although measurements form the groundwork for much of meteorology and more broadly the geosciences, student engagement and formal training is often limited. This is especially true at the undergraduate level. This is due the limited resources of time and finances: Undergraduates are busy, and instruments are expensive. Additionally, the physical scale of many instruments is such that they just cannot be brought “into” the classroom. While specific educational deployments are possible through the NCAR Lower Atmosphere Observing Facilities (LAOF) request

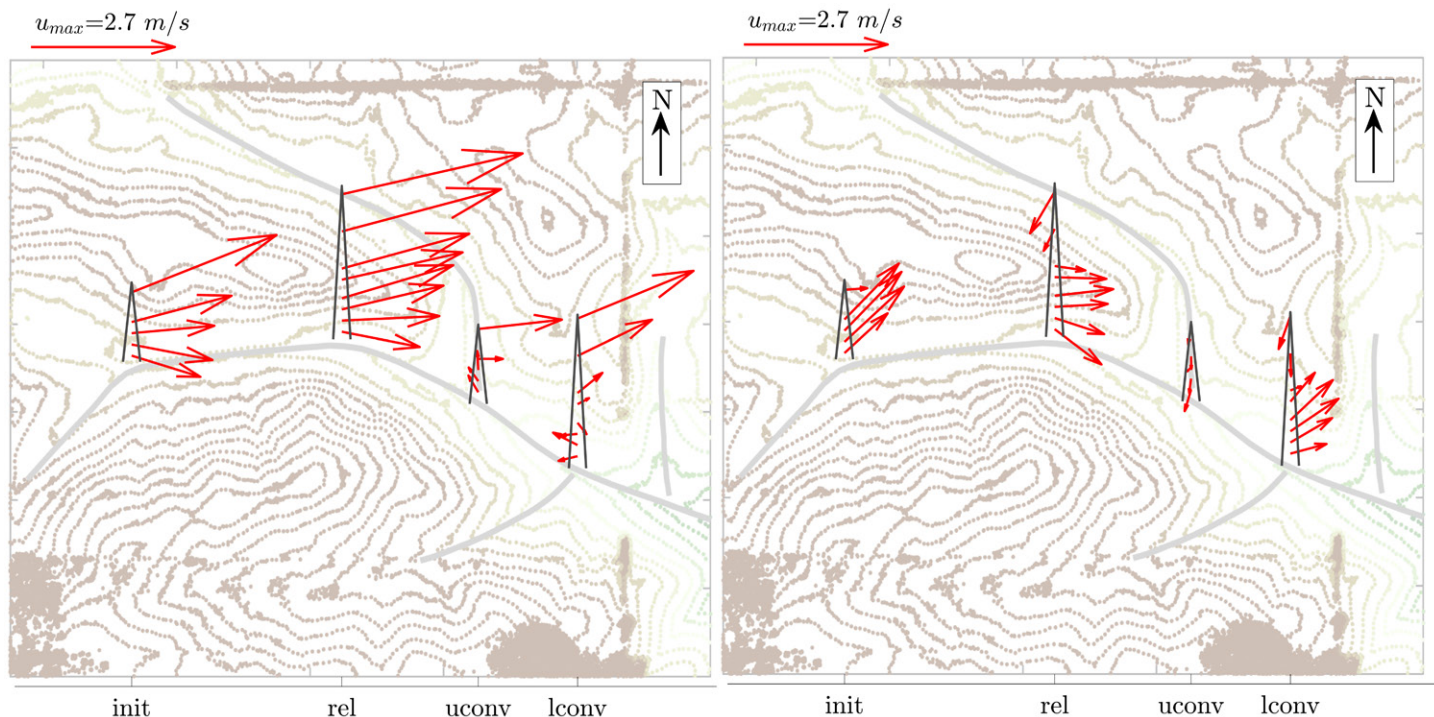


Fig. 10. Example convergence flows. (left) Convergence caused by drainage flow from initiation tower (init) and release tower (rel) hitting a stagnation area ( $0 \text{ m s}^{-1}$  wind speed below 10-m height) at upper convergence tower (uconv) and lower convergence tower (lconv). (right) Convergence caused by flow from feeder gully 1 at uconv to halt the along-gully flow (seen below 15-m height at other towers). The wind quivers are scaled with respect to the maximum velocity ( $2.7 \text{ m s}^{-1}$ ).

process, they require extreme dedication of individual or small groups of faculty to their teaching mission. This dedication can often be at the expense of their research mission, enforcing a separation between the “research” and “teaching” aspects. The SAVANT team experimented with several ways to overcome this separation and integrate teaching and research.

Traditional grant funding mechanisms were used to support assistantships for five graduate students who worked on the project prior to, during, and after the campaign. These students were all supported by National Science Foundation (NSF) funds, and some component of the work on the project supported their theses and/or dissertation work. Beyond that, all students were cross trained on the different instruments (lidar, radiosondes, CTEMPS, DustTraks, and OPCs) and deployment and data collection responsibilities were rotated between them. In this way, students were aware of the larger context of the project and the various logistical aspects of multi-instrument field deployments. During the campaign, students at both the graduate and undergraduate level were responsible for daily forecasts and maintaining an outlook grid. This was a vital part of the campaign and gave students a sense of ownership and responsibility, ultimately leading to better engagement of the students. This approach to incorporating education into the personnel needs of field project was successful. Additional coordination with program directors at the students’ home institutions was necessary to allow students to complete other course work and degree requirements while away from campus.

Outside of these more traditional student training activities, several opportunities were taken to leverage the field campaign as an educational resource. These opportunities were available due to the timing and location of the campaign. The fall timing overlapped with the fall semester at most U.S. universities, meaning it was easier to incorporate field visits, and guest lectures (in person and remote) into course syllabuses and learning objectives. The location, just outside of the Urbana–Champaign campus of the University of Illinois



allowed class visits to the field site. This was done in two different ways: single short site visits and semester long, campaign-centered instrumentation courses. These different instructional approaches impacted students at three different universities.

Site visits were done at both the undergraduate and graduate levels. Multiple undergraduate classes in both atmospheric science and engineering courses at the University of Illinois came to visit the site and learn about the different instruments, notably seeing all three lidars work. SAVANT was also used as the semester-long focus for a mixed-level course at the University of Wisconsin. This model was later used for a student course visit to the CHEESEHEAD campaign the following year (Butterworth et al. 2021). In these two cases, both courses were focused on measurements and instrumentation and the field campaigns were used as the central theme throughout the semester.

During SAVANT, a course of students from the University of Wisconsin visited the SAVANT field campaign in Illinois. “Meteorological Measurements” is an existing course at UW with an established history of field trips, so institutional buy-in and precedence existed. The trip was funded through an NSF supplemental award, in which UW unmanned aerial vehicles (UAV) based forward looking infrared (FLIR) instrumentation available from the University of Wisconsin could enhance the science objectives of SAVANT. The students traveled from Wisconsin to Illinois for a 2-night trip in October. During their stay, they deployed additional instruments on their own, participated in an IOP, and networked with SAVANT and NCAR personnel. After returning to UW, they authored a collaborative class paper reporting their results. This experience directly increased the course’s learning objectives of “providing exposure to more advanced surface layer instrumentation” and “improved teamwork skills by participating in a hands-on, team-based field project” (A. Desai 2019, personal communication).

## Outlook

The SAVANT dataset has the potential to answer many questions of the effects of shallow topography on the near-surface atmosphere. The campaign was successful in collecting data that will address the initial scientific objectives and others that have subsequently been identified. We show here the data products available, and an overview of the varied conditions sampled during the campaign. A significant portion of the data indicates potential for gully flow and can be analyzed to develop more sophisticated boundary layer theories. The data also contain detailed observations of specific terrain induced flows and unexpected conditions such as instances when drainage is offset from the gully and cases of up-gully flow.

We presented here a single technique for identifying drainage conditions. Although this initial presentation provides only a generalized characterization of the entire dataset, we conclude that consistent low wind speed favors drainage. This is further confirmed when

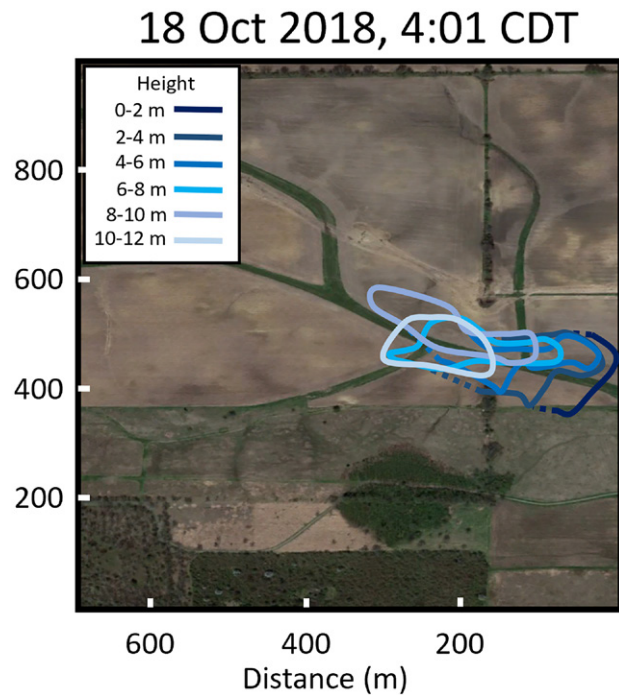


Fig. 11. “Topography” of the outer edges of the smoke plume on 18 Oct 2018, using Doppler lidar azimuthal scans starting at 0401 CDT. Data taken in at scans up to 10° elevation angle were grouped into 200-m intervals from the surface to 1200 m. No adjustment for movement of the plume during the azimuthal scans was made for this analysis.

examining our choice of criteria. We used here a threshold of a change in wind 10% higher than the background wind. This threshold was chosen arbitrarily to represent a noticeable change in wind speed. Thresholds of 20%, 30%, and 40% were also applied, and show no difference to the overall results. Each increase in threshold resulted in fewer periods being identified as drainage likely, and naturally shifted the average of the drainage-likely profiles shown in Fig. 4 to a slightly slower wind speed. Both convergence and drainage-like flows are present in short pulses under other wind conditions. Additionally, ambient winds do not need to be well aligned with the gully, indicating more complicated linkages between the micro- and meso-scales exist. A significant difference exists between preharvest and postharvest time periods, with flow separation and impacts of the gully effect more prominent when the canopy was present. Removal of canopy allows shallow slope to play a larger role in flow channelization.

Additional exploration of the dataset in terms of the hockey-stick similarity theory (HOST) recently discussed widely in the literature (Sun et al. 2020) further reveals the richness of the dataset, as well as the potential to improve upon our understanding of how HOST performs in converging flows. The SAVANT data here have much to contribute to this discussion, as changes in the HOST threshold velocity exist with different drainage potential. A more in-depth analysis of HOST as it relates to the roughness change is presented in Bhimireddy et al. (2022). Overall, pressure data indicate that waves initiated higher than the surface layer, and no correlations are yet to be found between local stability and gravity wave activity. Preliminary results from analysis of aerosol lidar data (Bhimireddy et al. 2021) and Dust-Trak plume concentrations indicate the tracer plume is dispersed differently in pulsing and converging flows. Finally, results indicate that new or enhanced parameterizations of the likelihood of drainage conditions in stable boundary layer can be developed. In particular, several other criteria to disentangle the differences between drainage and convergence are being explored for modeling purposes.

SAVANT also pushed the boundaries of near-surface spatial measurements with multiple lidar systems and the CTEMPS DTS system. The deployment of multiple lidars was quite successful and has identified new pathways to understand dispersive movement. However, to deploy multiple horizontal scanning lidars much consideration must be given to the initial locations, supporting infrastructure, and scanning routines. Lidars are also hard to deploy in narrow gullies and very careful alignment is required. High resolution scanning systems with a short overlap range are also needed to accomplish measurements of this nature. CTEMPS-DTS, while offering superior spatiotemporal resolution and sampling flexibility, is extremely difficult to deploy and maintain in the near-surface atmosphere. This was particularly true in a site where wildlife could not be easily controlled. We feel it is better suited for different measurements further above ground in these conditions. These spatiotemporal measurements, while providing many new scientific insights, remain difficult and labor intensive. Both these factors should be considered for all future field campaigns.

**Acknowledgments.** Funding for this study was provided from NSF Awards 17-33877 and 17-33746 and the Illinois State Water Survey at the University of Illinois at Urbana–Champaign. The authors thank UCAR staff and several students who participated during SAVANT and are responsible for generating the dataset. Opinions expressed are those of the authors and not necessarily those of the NSF, Illinois State Water Survey, the Prairie Research Institute, the University of Illinois, or the University of South Carolina. The authors declare that there is no conflict of interest. We thank CTEMPS, funded by the National Science Foundation (EAR Awards 18-32109 and 18-32170), for timely and effective provision of experimental design support, logistical support, and equipment for the project.

**Data availability statement.** All data used in this study are openly available from NCAR/EOL SAVANT data archive at <https://doi.org/10.26023/NKWR-EYWS-5JOW>.



## References

- Acevedo, O. C., and D. R. Fitzjarrald, 2003: In the core of the night—Effects of intermittent mixing on a horizontally heterogeneous surface. *Bound.-Layer Meteor.*, **106**, 1–33, <https://doi.org/10.1023/A:1020824109575>.
- , R. Maroneze, F. D. Costa, F. S. Puhales, G. A. Degrazia, L. G. Nogueira Martins, P. E. Soares de Oliveira, and L. Mortarini, 2019: The nocturnal boundary layer transition from weakly to very stable. Part I: Observations. *Quart. J. Roy. Meteor. Soc.*, **145**, 3577–3592, <https://doi.org/10.1002/qj.3642>.
- Andreas, E. L., L. Mahrt, and D. Vickers, 2012: A new drag relation for aerodynamically rough flow over the ocean. *J. Atmos. Sci.*, **69**, 2520–2537, <https://doi.org/10.1175/JAS-D-11-0312.1>.
- Arya, S. P., 2001: *Introduction to Micrometeorology*. 2nd ed. Academic Press, 420 pp.
- Balsley, B., D. Fritts, R. Frehlich, R. M. Jones, S. Vadas, and R. Coulter, 2002: Up-gully flow in the Great Plains region: A mechanism for perturbing the nighttime lower atmosphere? *Geophys. Res. Lett.*, **29**, 1931, <https://doi.org/10.1029/2002GL015435>.
- Basu, S., 2018: A simple recipe for estimating atmospheric stability solely based on surface-layer wind speed profile. *Wind Energy*, **21**, 937–941, <https://doi.org/10.1002/we.2203>.
- Bhimireddy, S. R., J. Wang, A. Hiscox, and D. A. Kristovich, 2021: Aerosol and Doppler lidar observations of nocturnal drainage flows in shallow gully topographies during the Stable Atmospheric Variability and Transport (SAVANT) field campaign. *11th Symp. on Lidar Atmospheric Applications*, Online, Amer. Meteor. Soc., 6.8., <https://ams.confex.com/ams/101ANNUAL/meetingapp.cgi/Paper/383706>.
- , —, —, and —, 2022: Influence of stability and surface roughness on turbulence during the Stable Atmospheric Variability and Transport (SAVANT) field campaign. *J. Appl. Meteor. Climatol.*, **61**, 1273–1289, <https://doi.org/10.1175/JAMC-D-21-0160.1>.
- Butterworth, B. J., and Coauthors, 2021: Connecting land–atmosphere interactions to surface heterogeneity in CHEESEHEAD19. *Bull. Amer. Meteor. Soc.*, **102**, E421–E445, <https://doi.org/10.1175/BAMS-D-19-0346.1>.
- Cheng, Y., Q. Li, A. Grachev, S. Argentini, H. J. S. Fernando, and P. Gentile, 2020: Power-law scaling of turbulence cospectra for the stably stratified atmospheric boundary layer. *Bound.-Layer Meteor.*, **177**, 1–18, <https://doi.org/10.1007/s10546-020-00545-6>.
- Clements, W. E., J. A. Archuleta, and D. E. Hoard, 1989: Mean structure of the nocturnal drainage flow in a deep valley. *J. Appl. Meteor.*, **28**, 457–462, [https://doi.org/10.1175/1520-0450\(1989\)028<0457:MSOTND>2.0.CO;2](https://doi.org/10.1175/1520-0450(1989)028<0457:MSOTND>2.0.CO;2).
- Cuxart, J., and Coauthors, 2000: Stable Atmospheric Boundary-Layer Experiment in Spain (SABLES 98): A report. *Bound.-Layer Meteor.*, **96**, 337–370, <https://doi.org/10.1023/A:1002609509707>.
- De Jong, S. A. P., J. D. Slingerland, and N. C. Van De Giesen, 2015: Fiber optic distributed temperature sensing for the determination of air temperature. *Atmos. Meas. Tech.*, **8**, 335–339, <https://doi.org/10.5194/amt-8-335-2015>.
- Doran, J. C., T. W. Horst, and C. D. Whiteman, 1990: The development and structure of nocturnal slope winds in a simple valley. *Bound.-Layer Meteor.*, **52**, 41–68, <https://doi.org/10.1007/BF00121377>.
- , J. D. Fast, and J. Horel, 2002: The VTMX 2000 campaign. *Bull. Amer. Meteor. Soc.*, **83**, 537–551, [https://doi.org/10.1175/1520-0477\(2002\)083<0537:TVC>2.3.CO;2](https://doi.org/10.1175/1520-0477(2002)083<0537:TVC>2.3.CO;2).
- Fernando, H. J. S., B. Verhoef, S. Di Sabatino, L. S. Leo, and S. Park, 2013: The Phoenix evening Transition Flow Experiment (TRANSFLEX). *Bound.-Layer Meteor.*, **147**, 443–468, <https://doi.org/10.1007/s10546-012-9795-5>.
- , and Coauthors, 2015: The MATERHORN: Unraveling the intricacies of mountain weather. *Bull. Amer. Meteor. Soc.*, **96**, 1945–1967, <https://doi.org/10.1175/BAMS-D-13-00131.1>.
- , and Coauthors, 2019: The Perdigão: Peering into microscale details of mountain winds. *Bull. Amer. Meteor. Soc.*, **100**, 799–819, <https://doi.org/10.1175/BAMS-D-17-0227.1>.
- Finnigan, J., and Coauthors, 2020: Boundary-layer flow over complex topography. *Bound.-Layer Meteor.*, **177**, 247–313, <https://doi.org/10.1007/s10546-020-00564-3>.
- Garrett, J. R., 1992: *The Atmospheric Boundary Layer*. Cambridge University Press, 396 pp.
- Gray, B., 2019: Weedkiller complaints skyrocket among Illinois farmers. *St. Louis Dispatch*, 22 December, [www.stltoday.com/business/local/weedkiller-complaints-skyrocket-among-illinois-farmers/article\\_8a8fe703-b973-52a8-89f7-42fa14f5ef12.html](http://www.stltoday.com/business/local/weedkiller-complaints-skyrocket-among-illinois-farmers/article_8a8fe703-b973-52a8-89f7-42fa14f5ef12.html).
- Grisogono, B., and J. Oerlemans, 2001: A theory for the estimation of surface fluxes in simple katabatic flows. *Quart. J. Roy. Meteor. Soc.*, **127**, 2725–2739, <https://doi.org/10.1002/qj.49712757811>.
- , J. Sun, and D. Belušić, 2020: A note on MOST and HOST for turbulence parametrization. *Quart. J. Roy. Meteor. Soc.*, **146**, 1991–1997, <https://doi.org/10.1002/qj.3770>.
- Gultepe, I., and Coauthors, 2016: An overview of the MATERHORN fog project: Observations and predictability. *Pure Appl. Geophys.*, **173**, 2983–3010, <https://doi.org/10.1007/s00024-016-1374-0>.
- Holtstlag, A. A. M., and Coauthors, 2013: Stable atmospheric boundary layers and diurnal cycles: Challenges for weather and climate models. *Bull. Amer. Meteor. Soc.*, **94**, 1691–1706, <https://doi.org/10.1175/BAMS-D-11-00187.1>.
- Hoover, J. D., D. R. Stauffer, S. J. Richardson, L. Mahrt, B. J. Gaudet, and A. Suarez, 2015: Submeso motions within the stable boundary layer and their relationships to local indicators and synoptic regime in moderately complex terrain. *J. Appl. Meteor. Climatol.*, **54**, 352–369, <https://doi.org/10.1175/JAMC-D-14-0128.1>.
- Kaiser, A., D. Faranda, S. Krumscheid, D. Belušić, and N. Vercauteren, 2020: Detecting regime transitions of the nocturnal and polar near-surface temperature inversion. *J. Atmos. Sci.*, **77**, 2921–2940, <https://doi.org/10.1175/JAS-D-19-0287.1>.
- Kurbatskii, A. F., and L. I. Kurbatskaya, 2011: The wind-field structure in a stably stratified atmospheric boundary layer over a rough surface. *Izv. Atmos. Ocean. Phys.*, **47**, 281–289, <https://doi.org/10.1134/S0001433811030091>.
- Lapo, K., B. Nijssen, and J. D. Lundquist, 2019: Evaluation of turbulence stability schemes of land models for stable conditions. *J. Geophys. Res. Atmos.*, **124**, 3072–3089, <https://doi.org/10.1029/2018JD028970>.
- Lee, T. R., and M. Buban, 2020: Evaluation of Monin–Obukhov and bulk Richardson parameterizations for surface–atmosphere exchange. *J. Appl. Meteor. Climatol.*, **59**, 1091–1107, <https://doi.org/10.1175/JAMC-D-19-0057.1>.
- Lemone, M. A., and Coauthors, 2018: 100 years of progress in boundary layer meteorology. *A Century of Progress in Atmospheric and Related Sciences: Celebrating the American Meteorological Society Centennial*, Meteor. Monogr., No. 59, Amer. Meteor. Soc., <https://doi.org/10.1175/AMSMONOGRAPHIS-D-18-0013.1>.
- Lothorn, M., and Coauthors, 2014: The BLLAST field experiment: Boundary-Layer Late Afternoon and Sunset Turbulence. *Atmos. Chem. Phys.*, **14**, 10931–10960, <https://doi.org/10.5194/acp-14-10931-2014>.
- Mahrt, L., 2017: Stably stratified flow in a shallow valley. *Bound.-Layer Meteor.*, **162** (1), 1–20, <https://doi.org/10.1007/s10546-016-0191-4>.
- , J. Sun, W. Blumen, T. Delany, and S. Oncley, 1998: Nocturnal boundary-layer regimes. *Bound.-Layer Meteor.*, **88**, 255–278, <https://doi.org/10.1023/A:1001171313493>.
- , S. Richardson, N. Seaman, and D. Stauffer, 2010: Non-stationary drainage flows and motions in the cold pool. *Tellus*, **62A**, 698–705, <https://doi.org/10.1111/j.1600-0870.2010.00473.x>.
- , —, —, and —, 2012: Turbulence in the nocturnal boundary layer with light and variable winds. *Quart. J. Roy. Meteor. Soc.*, **138**, 1430–1439, <https://doi.org/10.1002/qj.1884>.
- , —, D. Stauffer, and N. Seaman, 2014a: Nocturnal wind-directional shear in complex terrain. *Quart. J. Roy. Meteor. Soc.*, **140**, 2393–2400, <https://doi.org/10.1002/qj.2369>.
- , J. Sun, S. P. Oncley, and T. W. Horst, 2014b: Transient cold air drainage down a shallow valley. *J. Atmos. Sci.*, **71**, 2534–2544, <https://doi.org/10.1175/JAS-D-14-0010.1>.

- , —, and D. Stauffer, 2015: Dependence of turbulent velocities on wind speed and stratification. *Bound.-Layer Meteor.*, **155**, 55–71, <https://doi.org/10.1007/s10546-014-9992-5>.
- Medeiros, L. E., and D. R. Fitzjarrald, 2014: Stable boundary layer in complex terrain. Part I: Linking fluxes and intermittency to an average stability index. *J. Appl. Meteor. Climatol.*, **53**, 2196–2215, <https://doi.org/10.1175/JAMC-D-13-0345.1>.
- Miller, D. R., L. R. Khot, A. L. Hiscox, M. Salyani, T. W. Walker, and M. Farooq, 2012: Effect of atmospheric conditions on coverage of fogger applications in a desert surface boundary layer. *Trans. ASABE*, **55**, 351–361, <https://doi.org/10.13031/2013.41373>.
- Mortarini, L., M. Stefanello, G. Degrazia, D. Roberti, S. Trini Castelli, and D. Anfossi, 2016: Characterization of wind meandering in low-wind-speed conditions. *Bound.-Layer Meteor.*, **161**, 165–182, <https://doi.org/10.1007/s10546-016-0165-6>.
- Nadeau, D. F., E. R. Pardyjak, C. W. Higgins, H. Huwald, and M. B. Parlange, 2013: Flow during the evening transition over steep Alpine slopes. *Quart. J. Roy. Meteor. Soc.*, **139**, 607–624, <https://doi.org/10.1002/qj.1985>.
- NCAR/EOL, 2021: NCAR/EOL ISFS surface meteorology and flux products, 5-minute, geographic coordinate and tilt corrected winds, version 2.0. UCAR/NCAR Earth Observing Laboratory, accessed 10 October 2021, <https://doi.org/10.26023/NKWR-EYWS-5J0W>.
- Optis, M., A. Monahan, and F. C. Bosveld, 2014: Moving beyond Monin–Obukhov similarity theory in modelling wind-speed profiles in the lower atmospheric boundary layer under stable stratification. *Bound.-Layer Meteor.*, **153**, 497–514, <https://doi.org/10.1007/s10546-014-9953-z>.
- Pardyjak, E. R., and L. S. Leo, 2020: Preface: Special issue on the MATERHORN program and complex terrain flows. *Environ. Fluid Mech.*, **20**, 1173–1175, <https://doi.org/10.1007/s10652-020-09772-4>.
- Pfister, L., K. Lapo, C. Sayde, J. Selker, L. Mahrt, and C. K. Thomas, 2019: Classifying the nocturnal atmospheric boundary layer into temperature and flow regimes. *Quart. J. Roy. Meteor. Soc.*, **145**, 1515–1534, <https://doi.org/10.1002/qj.3508>.
- , —, L. Mahrt, and C. K. Thomas, 2021a: Thermal submesoscale motions in the nocturnal stable boundary layer. Part 1: Detection and mean statistics. *Bound.-Layer Meteor.*, **180**, 187–202, <https://doi.org/10.1007/s10546-021-00618-0>.
- , —, —, and —, 2021b: Thermal submeso motions in the nocturnal stable boundary layer. Part 2: Generating mechanisms and implications. *Bound.-Layer Meteor.*, **180**, 203–224, <https://doi.org/10.1007/s10546-021-00619-z>.
- Poulos, G. S., and Coauthors, 2002: CASES-99: A comprehensive investigation of the stable nocturnal boundary layer. *Bull. Amer. Meteor. Soc.*, **83**, 555–582, [https://doi.org/10.1175/1520-0477\(2002\)083<0555:CACIOT>2.3.CO;2](https://doi.org/10.1175/1520-0477(2002)083<0555:CACIOT>2.3.CO;2).
- Riley, S. J., S. D. DeGloria, and R. Elliot, 1999: A terrain ruggedness index that quantifies topographic heterogeneity. *Intermt. J. Sci.*, **5**, 23–27.
- Sappington, J. M., K. M. Longshore, and D. B. Thompson, 2007: Quantifying landscape ruggedness for animal habitat analysis: A case study using bighorn sheep in the Mojave Desert. *J. Wildl. Manage.*, **71**, 1419–1426, <https://doi.org/10.2193/2005-723>.
- Smith, R. B., 2019: 100 years of progress on mountain meteorology research. *A Century of Progress in Atmospheric and Related Sciences: Celebrating the American Meteorological Society Centennial*, Meteor. Monogr., No. 59, Amer. Meteor. Soc., <https://doi.org/10.1175/AMSMONOGRAPHIS-D-18-0022.1>.
- Soler, M. R., C. Infante, P. Buenestado, and L. Mahrt, 2002: Observations of nocturnal drainage flow in a shallow gully. *Bound.-Layer Meteor.*, **105**, 253–273, <https://doi.org/10.1023/A:1019910622806>.
- Stiperski, I., and M. Calaf, 2018: Dependence of near-surface similarity scaling on the anisotropy of atmospheric turbulence. *Quart. J. Roy. Meteor. Soc.*, **144**, 641–657, <https://doi.org/10.1002/qj.3224>.
- , —, and M. W. Rotach, 2019: Scaling, anisotropy, and complexity in near-surface atmospheric turbulence. *J. Geophys. Res. Atmos.*, **124**, 1428–1448, <https://doi.org/10.1029/2018JD029383>.
- Stull, R., 2001: *An Introduction to Boundary Layer Meteorology*. Kluwer Academic, 670 pp.
- Sun, J., L. Mahrt, C. Nappo, and D. H. Lenschow, 2015: Wind and temperature oscillations generated by wave–turbulence interactions in the stably stratified boundary layer. *J. Atmos. Sci.*, **72**, 1484–1503, <https://doi.org/10.1175/JAS-D-14-0129.1>.
- , D. H. Lenschow, M. A. Lemone, and L. Mahrt, 2016: The role of large-coherent-eddy transport in the atmospheric surface layer based on CASES-99 observations. *Bound.-Layer Meteor.*, **160**, 83–111, <https://doi.org/10.1007/s10546-016-0134-0>.
- , E. S. Takle, and O. C. Acevedo, 2020: Understanding physical processes represented by the Monin–Obukhov bulk formula for momentum transfer. *Bound.-Layer Meteor.*, **177**, 69–95, <https://doi.org/10.1007/s10546-020-00546-5>.
- Svensson, G., and A. A. M. Holtslag, 2009: Analysis of model results for the turning of the wind and related momentum fluxes in the stable boundary layer. *Bound.-Layer Meteor.*, **132**, 261–277, <https://doi.org/10.1007/s10546-009-9395-1>.
- Tong, C., and M. Ding, 2019: Multi-point Monin–Obukhov similarity in the convective atmospheric surface layer using matched asymptotic expansions. *J. Fluid Mech.*, **864**, 640–669, <https://doi.org/10.1017/jfm.2019.38>.
- USEPA, 2022: Models for pesticide risk assessment. USEPA, [www.epa.gov/pesticide-science-and-assessing-pesticide-risks/models-pesticide-risk-assessment](http://www.epa.gov/pesticide-science-and-assessing-pesticide-risks/models-pesticide-risk-assessment).
- van de Wiel, B. J. H., A. F. Moene, and H. J. J. Jonker, 2012a: The cessation of continuous turbulence as precursor of the very stable nocturnal boundary layer. *J. Atmos. Sci.*, **69**, 3097–3115, <https://doi.org/10.1175/JAS-D-12-064.1>.
- , —, —, P. Baas, S. Basu, J. M. M. Donda, J. Sun, and A. A. M. Holtslag, 2012b: The minimum wind speed for sustainable turbulence in the nocturnal boundary layer. *J. Atmos. Sci.*, **69**, 3116–3127, <https://doi.org/10.1175/JAS-D-12-0107.1>.
- Vassallo, D., R. Krishnamurthy, R. Menke, and H. J. S. Fernando, 2021: Observations of stably stratified flow through a microscale gap. *J. Atmos. Sci.*, **78**, 189–208, <https://doi.org/10.1175/JAS-D-20-0087.1>.
- Whiteman, C. D., 2000: *Mountain Meteorology*. Oxford University Press, 355 pp.
- Wulfmeyer, V., and Coauthors, 2018: A new research approach for observing and characterizing land–atmosphere feedback. *Bull. Amer. Meteor. Soc.*, **99**, 1639–1667, <https://doi.org/10.1175/BAMS-D-17-0009.1>.
- Yus-Díez, J., M. Udina, M. R. Soler, M. Lothon, E. Nilsson, J. Bech, and J. Sun, 2019: Nocturnal boundary layer turbulence regimes analysis during the BLLAST campaign. *Atmos. Chem. Phys.*, **19**, 9495–9514, <https://doi.org/10.5194/acp-19-9495-2019>.